First-principles survey of the structure, formation energies, and transition levels of As-interstitial defects in InGaAs

S. R. Lee, A. F. Wright, N. A. Modine, C. C. Battaile, S. M. Foiles, J. C. Thomas, and A. Van der Ven

Phys. Rev. B **92**, 045205 — Published 14 July 2015

DOI: 10.1103/PhysRevB.92.045205

A first-principles survey of the structure, formation energies, and transition levels of As-interstitial defects in InGaAs

S. R. Lee,[a] A. F. Wright, N. A. Modine, C. C. Battaile, and S. M. Foiles
Sandia National Laboratories, Albuquerque, NM 87185-1086, USA

J. C. Thomas
Materials Department, University of California, Santa Barbara, California 93106, USA

A. Van der Ven
Materials Department, University of California, Santa Barbara, California 93106, USA

ABSTRACT

While point defects in elemental (Si) and compound (GaAs, GaN, AlN) semiconductors have been extensively studied both experimentally and theoretically, only limited theoretical studies of these defects exist for technologically important binary (Si_xGe_{1-x}) and pseudo-binary ($In_xGa_{1-x}As$, $In_xGa_{1-x}N$, $Al_xGa_{1-x}N$) semiconductor alloys. Here, we use density-functional theory (DFT) and a recently developed bounds-analysis approach to survey the atomic structures, formation energies, and charge-state transition levels of the stable and metastable states of As interstitials in the pseudo-binary alloy $In_{0.5}Ga_{0.5}As$. Our studies consider seven different candidate defect structures for the As interstitial, with calculations performed for selected defect charge states in the range q=-2 to q=+3. In each case, the mean and standard deviation of the defect formation energy are determined using statistical sampling methods that place the defect into a wide variety of differing local-alloy environments. When examined from the point of view of the mean formation energy of the defect, the stable configurations of the As interstitial in $In_{0.5}Ga_{0.5}As$ are found to resemble previous findings for GaAs, with a C_{1h}-$p001_{III}$ interstitial structure in a q=+1 charge state favored near mid-gap and below, and a C_{2v}-110_a split-interstitial structure in a q=-1 charge state favored above mid-gap (the named point-group symmetries refer to the underlying symmetry that the alloy defect would possess if within GaAs). The statistical sampling reveals a strong dependence of the defect formation energy on the local alloy environment, with the standard deviation, σ, of the formation energy approaching 0.21 eV for the most stable As-interstitial structures. Because the range of ground-state

energies encountered by an As interstitial defect when moving through the alloy is found to be quite large, approaching ~ 1.2 eV ($\pm 3\sigma$), defect-diffusion pathways in $In_{0.5}Ga_{0.5}As$ will have spatial and temporal complexities not found in GaAs.

[a)]Electronic mail: srlee@sandia.gov

I. INTRODUCTION

Semiconductor alloys underpin a variety of important technologies, with SiGe alloys enabling strained-Si-based microprocessors, with InGaAs and InGaP alloys enabling optoelectronics-based telecommunications, with InGaN alloys enabling solid-state lighting, and with AlGaN alloys positioned to enable further advances in power electronics. Point-defect behavior in these alloys may be influenced by not only materials synthesis, but also subsequent device fabrication and processing, as well as end use of said devices. For example, as-grown point-defect content may limit the electronic or optoelectronic performance of alloys through mechanisms such as carrier scattering, carrier recombination, and dopant compensation. Similarly, ion implantation, thermal annealing, plasma-based etching, and other device-fabrication processes may alter as-grown defect populations or introduce new defects that again limit performance. Point-defect introduction or modification may also be important during device use, through long-term device aging, through use of devices in demanding thermal environments, or through exposure of devices to ionizing radiation in space or particle-accelerator-based applications.

Given the broad importance of point defects in semiconductor alloys, theoretical studies of these defects using first-principles methods remains scant, with only a few studies extant for each of the major semiconductor-alloy systems: SiGe [1, 2], InGaAs [3-6], GaAsP [7], InGaN [8], AlGaN [9], and dilute GaN:P [10]. Existing first-principles studies of defects in InGaAs bulk alloys, which are the focus of this paper, have considered only Ga and As vacancies and antisites [3-6]. The early InGaAs work of Bonapasta *et al.* uses density functional theory (DFT) in the local-density approximation (LDA) and places defect structures into 64-atom alloy supercells alloys with randomly populated cation sites [3]. Subsequent work by Murphy *et al.* uses DFT in the generalized-gradient approximation and also places defects into 64-atom supercells, but uses special quasirandom structures to simulate alloy randomness [4]. A recent study by Komsa and Pasquarello also uses a randomly populated 64-atom supercell. Notably, this group uses the improved performance of present-day computing clusters to apply more rigorous hybrid functional methods to defects in alloys for perhaps the first time [5]. In a departure from these studies based on periodic supercells and plane-wave basis sets, recent calculations by Bezyazychnaya *et al.* instead use self-consistent-field linear-combination-of-atomic-orbitals methods to study 70-atom,

randomly populated clusters, which are surface-passivated with hydrogen [6].

Here, we use DFT/LDA to study the atomistic structure, formation energies, and charge-state transition levels of previously unstudied As interstitials in $In_{0.5}Ga_{0.5}As$. Our long-term goal is to determine a broad set of InGaAs-alloy defect properties, as needed to enable continuum modelling of the transport and reaction of defects created by radiation-induced displacement-damage cascades in InGaAs-based heterojunction bipolar transistors (HBTs). Such models have been extensively pursued for Si and GaAs [11,12], but limited knowledge of defects in alloys hinders extension to InGaAs-based HBTs. Notably, these device-specific modeling needs, combined with a general lack of defect data in the alloys, drive our focus on InGaAs alloys even though DFT/LDA for $In_{0.5}Ga_{0.5}As$ features a larger-than-typical band-gap error. Our interest in defect transport immediately following radiation-damage events produces a focus on *highly non-equilibrium* defect populations, with the effect of alloying on such populations taking on particular importance. Within this context, the importance of As interstitials stems from their reputation as the most mobile of the intrinsic defects in GaAs, which causes them to dominate defect transport at short time scales following displacement-induced radiation-damage events [12, 13]. A similar importance is expected in displacement-damaged devices utilizing InGaAs alloys.

The body of the paper is organized as follows: Section II reports our DFT computational methods, details the seven candidate defect structures that are considered for the As interstitial, and describes how these structures are statistically implemented in $In_{0.5}Ga_{0.5}As$ alloy supercells. This section also briefly summarizes our recently developed bounds-analysis approach [14, 15], which we will apply in Section III to assess the validity, within the framework of the DFT calculations, of proposed charge states and defect structures found to be stable by the calculations. Section III reports and discusses our computational results for As interstitials in $In_{0.5}Ga_{0.5}As$. When considering only the mean defect-formation energy of the alloy, the most important ground-state structures and charge states of the As interstitial in $In_{0.5}Ga_{0.5}As$ are found to resemble to those of GaAs. In contrast to GaAs, however, the formation energy for a given defect varies quite strongly with the local alloy environment, with local variations in group-III sub-lattice occupancy producing a range of formation energies spanning more than l eV. Depending on the defect structure, these large variations in energy are found to produce spontaneous local changes in the As-

interstitial structure that would not be expected based on consideration of mean defect-formation energies alone. Finally, Section IV concludes with a summary of the work.

II. METHODS

A. Construction of candidate As-interstitial structures in $In_{0.5}Ga_{0.5}As$

DFT studies focused on a computational survey of the possible stable and metastable defect structures that may exist for the As interstitial in $In_{0.5}Ga_{0.5}As$. Figure 1 shows ball-and-stick models [16] of the specific defect structures that were considered. As shown in the figure, multiple defect charge states, q, selected from the range q=-2 to q=+3 were examined for each defect structure. These candidate structures are InGaAs-alloy analogues of similar As-interstitial defects in GaAs previously studied by Schultz *et al.* [13], and recently in more detail, by Wright and Modine [17]. The first part of the naming convention of the pictured alloy defects is based on the point symmetry (C_{2v}, C_{1h}, etc.) that the defect *would have in GaAs*, with all group-III sites occupied by Ga and with the defect structure properly symmetrized. The second part is based on the local geometric orientation, geometric character, and/or atomic character of the defect structure (110_a, $p001_{III}$, hex, III, etc.). Reference [13] gives further details of the defect naming convention as it originally appeared for describing intrinsic defects in GaAs. While we will be succinctly referring to these defects in terms of their geometric similarity to the nearest underlying GaAs symmetry, in no case does the named point symmetry rigorously exist because of the symmetry breaking brought about by alloying.

Since the defect formation energy in an InGaAs alloy is a strong function of the occupation of group-III lattice sites [4], calculations for each defect were carried out using large sets of differing alloy supercells wherein statistical sampling techniques were used to occupy the group-III sub-lattice. As seen in Fig. 1, each defect has either 3, 4, or 6 nearest neighbors on the group-III sub-lattice. For the majority of structures having 4 nearest neighbors, the nearest neighbor sites are considered in combination with the underlying defect pseudo-symmetry to define either 9 or 12 unique first-neighbor site-occupancy configurations about the defect. For each unique configuration of the group-III nearest neighbors, 6 different 217-atom supercells (216 bulk-like atoms plus the As interstitial) were constructed by randomly

occupying, with either an In or a Ga atom, each of the group-III sites positioned beyond the first neighbors. This combined sampling of the occupancies of the nearest neighbor and remaining group-III sites produced either 54 or 72 initial alloy configurations for each type of candidate defect structure [18]. The initial atomic positions of each defect type when inserted into the alloyed supercell were based on relative interstitial-As coordinates found in DFT calculations for the same type of defect in GaAs.

B. DFT calculations and convergence studies

DFT calculations were performed using the Socorro code [19] and the local-density approximation (LDA) for exchange and correlation [20-22]. Semilocal norm-conserving pseudopotentials (NCPs) for Ga^{+3} and As^{+5} were constructed using the FHI98PP code [23], and then converted into a local potential plus Kleinman-Bylander projectors [24] for use in Socorro. Semilocal NCPs for In^{+3} were constructed using the GNCPP code of Hamann [25], and then converted into a local potential plus Kleinman-Bylander projectors. Non-linear core corrections [26] were used in all of the NCPs. A 35 Ryd cutoff was used to define the plane wave basis for the Kohn-Sham orbitals and the Kleinman-Bylander projectors, and a 140 Ryd cutoff was used to define the plane wave basis [27] for the electron density and the local potentials. Sampling meshes in the Brillouin zone (denoted $n \times n \times n$, where n is an integer) were constructed using the Monkhorst-Pack technique [28], and the occupations of the Kohn-Sham orbitals at these sampling points were calculated using the Kohn-Sham eigenvalues and a Fermi function with kT = 25.7 meV, corresponding to room temperature. The convergence criterion for self-consistent electronic-structure simulations required the total energy of the supercell to be refined to $< 1.4 \times 10^{-6}$ eV between consecutive electronic iterations, and the convergence criterion for relaxation of the atomic coordinates of supercell atoms required the rms force on all atoms in the supercell to be refined to $< 5 \times 10^{-3}$ eV/nm. DFT calculations were implemented using a periodic-supercell representation and always included a full structural relaxation of the supercell. To obtain well-defined solutions to the Poisson equation for non-zero charge states, a uniform compensating charge density was added to all supercells containing charged defects [29].

Multiple plane-wave cutoffs for the Kohn-Sham orbitals (from 272 to 1088 eV) were used to estimate uncertainties in defect formation energies due to the cutoff energy. Formation energies for neutral and charged defect states contained within a specific configurational instance of the alloyed

supercell were found to be converged within ~0.05 eV for the selected orbital cutoff of 476 eV. In the convergence studies, electron-density cutoffs were always four times the orbital cutoffs. Convergence of charge-state transition levels was much smaller than the noted 0.05 eV because substantial cancellation of correlated formation-energy convergence errors occurs when differencing to obtain the transition levels. Multiple sampling meshes (from 1×1×1 up to 5×5×5) were used to assess uncertainties in defect formation energies due to Brillouin-zone sampling. For the 216-atom supercells used herein, formation energies were found to be converged to within ~0.02 eV with respect to the selected 3×3×3 k-point sampling mesh.

C. Benchmark calculations for GaAs, InAs, $In_{0.5}Ga_{0.5}As$, and As

To validate the NCPs, calculations were performed for the equilibrium lattice constants of zinc blende GaAs and InAs in 2-atom primitive supercells. For GaAs, energies were calculated for eleven lattice constants ranging from 5.345 Å to 5.874 Å and fit using the Murnaghan equation [30]. Consistent with trends found when using the LDA, the fit yielded a lattice constant of 5.605 Å, which is 0.8% smaller than the measured value at room temperature (5.653 Å). For InAs, energies were calculated for eleven lattice constants ranging from 5.768 Å to 6.350 Å and fit using the Murnaghan equation. Consistent with trends found when using the LDA, the fit yielded a lattice constant of 6.020 Å, which is 0.6% smaller than the measured value at room temperature (6.058 Å) [32].

To calculate the equilibrium lattice constant for an $In_{0.5}Ga_{0.5}As$ alloy, a 216-atom supercell was used wherein the group-III lattice sites were randomly populated with Ga or In, with the global composition of the supercell constrained to x=0.5. Energies were calculated using a 3×3×3 Monkhorst-Pack mesh for eleven supercell lattice constants ranging from 3×5.521 Å to 3×6.050 Å, which were again fit using the Murnaghan equation. The fit yielded a lattice constant of 3×5.808 Å, where the underlying 8-atom fcc lattice constant of 5.808 Å is 0.8 % smaller than the 5.856 Å lattice constant obtained by linear interpolation of the measured values for GaAs and InAs. The various random-alloy supercells constructed as described in Section II.A were each constrained to the equilibrium lattice constant computed here for the $In_{0.5}Ga_{0.5}As$ alloy.

The atomic chemical potential, μ_{As}, needed for calculating defect formation energies, was obtained

from separate DFT calculations for bulk arsenic in a rhombohedral A7 structure using a 24×24×24 sampling mesh. The hexagonally transformed lattice constants were found to be a = 3.741 Å and c = 10.131 Å, which are 0.5% and 3.0% smaller than the measured values [33].

D. Calculation of defect formation energies and transition levels

For a given defect structure and supercell size, the formation energy is calculated from DFT simulation results using the well-known expression [34-36]

$$E_f^D\left[q,L,E_F\right]=E^D\left[q,L\right]-E^B\left[0,L\right]-\sum_i n_i\mu_i+qE_F\ , \tag{1}$$

where $E^D(q,L)$ is the minimum energy of a defect D in a supercell of size L with charge state q, with L taken to be the cube root of the supercell volume; $E^B(0,L)$ is the energy of a neutral bulk supercell of the same size as the defect supercell; n_i is the number of atoms of type i that were added to ($n_i > 0$) or removed from ($n_i < 0$) the bulk supercell to form the defect structure; μ_i is the chemical potential of the reservoir providing atomic exchange for atoms i; and E_F is the Fermi level. The Fermi level is defined in terms of the chemical potential of the reservoir providing electron exchange, μ_e, and a *relative Fermi level*, ε_F, such that $E_F \equiv \mu_e+\varepsilon_F$. Herein, we will use the traditional convention in which $\mu_e=\varepsilon_{VBE}$, where ε_{VBE} is the Kohn-Sham eigenvalue at the valence-band edge. With this convention in mind, Eq. (1) may be rewritten for the specific case of the As interstitial in InGaAs:

$$E_f^D\left[q,L,\varepsilon_F\right]=E^D\left[q,L\right]-E^B\left[0,L\right]-\mu_{As}+q\left(\varepsilon_{VBE}+\varepsilon_F\right)\ . \tag{2}$$

For a given defect structure and supercell size, the energy level, $\varepsilon^D(q\text{-}1/q,L)$, for a transition between charge states $q-1$ and q is defined as the Fermi level at which the formation energies of the two charge states of defect D are equal [36]:

$$\varepsilon^D\left(q-1/q,L\right)=E_f^D\left[q-1,L,\varepsilon_F=0\right]-E_f^D\left[q,L,\varepsilon_F=0\right]\ . \tag{3}$$

For comparison to the bounds on defect transition levels to be discussed in the next section, we note that equation (3) can be rewritten in terms of supercell energies as [37, 38],

$$\varepsilon^D\left(q-1/q,L\right)=E^D\left(q-1,L\right)-E^D\left(q,L\right)-\varepsilon_{VBE}\ . \tag{4}$$

E. Calculation of bounds on defect transition levels

Once DFT calculations for the candidate charge states and defect structures are completed, an analysis must be performed to distinguish defect-related charge states from delocalized bulk-related states. We proceed using a recently developed approach where defect levels are compared to *thermodynamically derived bounds on the defect levels*, with the bounds defined as follows [14]: For a defect supercell of size L, the *upper bound* is the energy to add one electron to a bulk supercell of size L,

$$\varepsilon^B(-1/0,L) = E^B(-1,L) - E^B(0,L) - \varepsilon_{VBE} \ , \tag{5}$$

and the *lower bound* is the energy to remove one electron from a bulk supercell of size L,

$$\varepsilon^B(0/+1,L) = E^B(0,L) - E^B(+1,L) - \varepsilon_{VBE} \ , \tag{6}$$

where we reference the bounds to ε_{VBE} for consistency with the defect levels shown in Eqs. 3 and 4. To better appreciate the limiting relationship that these bounds place upon defect transition levels, one might note that the bounds can be heuristically derived by simply replacing the total defect energy, $E^D[q,L]$, in Eq. 2 with the total energy of a charged bulk supercell, $E^B[q,L]$, yielding by analogy the formation energy of the charged bulk supercell, $E_f^B[q,L,\varepsilon_F]$. By replacing both instances of E_f^D with E_f^B in Eq. (3) for the defect transition level, and by then considering the cases q=0 and q=+1, one continues the analogy thereby recovering the upper and lower bounds in the guise of bulk transition levels. Through this analogy, we thus see that the upper bound approximates the level at which an electron added to a defect supercell goes into a delocalized conduction-band state instead of a localized defect state, and the lower bound approximates the level at which an electron removed from the defect supercell comes out of a delocalized valence-band state instead of a localized defect state. The bounds are approximate because the volume of the bulk-like region in a defect-containing supercell is less than the supercell volume. Consequently, as the supercell size increases the bounds become less approximate [14].

We plot calculated bounds [39] in $In_{0.5}Ga_{0.5}As$ as a function of supercell size in Fig. 2. The solid-black symbols plot the bounds computed for supercells ranging in size from 21600 atoms down to < 12 atoms, with the supercell size shown on the upper axis. The solid-black lines are smoothed interpolations of the resulting series of bounds calculations, and for reference, the blue-dashed lines plot the Kohn-Sham band gap. The lower axis shows the corresponding charge densities, ranging from $1.9\text{x}10^{18}$ to $3.8\text{x}10^{21}$

cm^{-3}, that result when adding one electron to (or removing one electron from) each supercell. Because of Burstein-Moss band-filling effects [40, 41] caused by adding or removing charge from the *finite-sized* supercells, the upper bounds always lie above the Kohn-Sham gap and the lower bounds always lie below the Kohn-Sham gap. The upper bounds deviate more strongly from the Kohn-Sham band edge than the lower bounds because of the smaller effective mass and lower density of states for the conduction band, which enables higher band filling for a given charge density. As the supercell size approaches infinity and band filling decreases, we see the bounds approach the Kohn-Sham band edges [14].

For the 216-atom supercells used in this study, the difference in the bounds – and thus the maximal range of accessible defect levels – is seen to exceed the Kohn-Sham band gap by a very large 0.80 eV. Notably, it is this band-filling-induced enlargement of the finite supercell's apparent band gap to ≈0.92 eV -- well above the very small Kohn-Sham band gap of ≈0.12 eV for $In_{0.5}Ga_{0.5}As$ -- that makes semi-local DFT studies of point defects in these alloys possible in the presence of the large band-gap error inherent to semi-local functionals. As shown in Fig. 2, there is good agreement between the apparent gap of the finite 216-atom alloyed supercell (0.92 eV) and the measured band gap [42] of unstrained $In_{0.5}Ga_{0.5}As$ at 4 K (0.846 eV). This agreement is simply a fortuitous result of higher band filling for small supercells. Such agreement tends to persist at small supercells sizes (~32-216 atoms) for the bounds calculated for a variety of semiconductors, explaining why semilocal DFT finds levels that span the experimental gap [14].

While these are interesting observations, the most important use of the bounds is to compare them to calculated DFT transition levels in order to distinguish localized defect-related charge states from delocalized band-edge-related states, thereby identifying the admissible localized charge states of our candidate defect structures [14,15]. When comparing a candidate DFT defect level to the bounds for a given supercell size, one of three specific cases will result: (1) the defect level will fall within not only the bounds, but also within the Kohn-Sham gap; (2) the level will fall outside the Kohn-Sham gap but remain within the bounds; or (3) the level will equal or exceed one of the bounds. The most likely interpretation of each case may be summarized as follows. In Case 1, the defect strongly localizes charge for both charge states associated with the level. In Case 2, the charge partially delocalizes for at least one of the

charge states of the level. Moreover, the degree of delocalization may be estimated using the supercell-size dependence of the bounds. To make this estimate, one determines the added (or removed) charge density at which one of the bounds is equal to the level in question (using the dependence of the bounds on charge density shown in Fig. 2); one then divides this assessment of delocalized charge density by the total added (or removed) charge density for the candidate level and supercell size. Such calculations show the amount of delocalization to be small (< 10-20%) for most defect levels falling under Case 2, excepting those levels that begin to approach the bounds. In Case 3, the added (or removed) charge is fully delocalized for at least one of the two charge states of the level, and the state that clearly involves delocalized charge is inadmissible and should be eliminated from further consideration. If the level is at the upper bounds, the more negative defect state is the one eliminated, and if the level is at the lower bounds, the more positive defect state is the one eliminated. Those Case-2 defect levels whose approach to the bounds produces a large estimated fraction of delocalized charge are treated similarly to Case 3. In certain instances, a defect level may involve a genuine hydrogenic state having a charge distribution weakly localized at the defect while nonetheless exhibiting Case-1 or Case-2 behavior; analysis of such instances requires detailed comparison of the level to the bounds as a function of supercell size, as discussed elsewhere [14, 15]. Specific examples of the described bounds-analysis approach will be given in Section III.B.

F. Effects of finite supercell size

Once admissible defects with strongly localized charge distributions have been identified in the bounds analysis, post-processing steps may be applied to remove finite-supercell-size effects and estimate defect properties in the dilute limit [43-52]. These finite-size effects are most significant for higher defect charge states and arise from spurious electrostatic interactions of the charged defect with its periodic images and neutralizing background charge [43, 44]. Pending adaptation of these finite-size correction methods to our statistical studies of alloys, we will rely herein on results from recent supercell-size-dependent studies of As interstitials in GaAs [17] to gauge the likely importance of these corrections for our similar As interstitials in InGaAs. Given that electrostatic finite-size corrections scale inversely with the static dielectric constant [43,44], ε, and noting that ε is quite similar for GaAs and $In_{0.53}Ga_{0.47}As$

(13.18 vs. 13.94) [53], one may infer that finite-size corrections in $In_xGa_{1-x}As$-alloy supercells with x near 0.5 will resemble those already found for the corresponding As-interstitials in GaAs. The GaAs-based estimate of such corrections [17] and their implications for present results will be given on a case-by-case basis for each valid defect identified during the bounds analysis. We report only uncorrected formation energies and levels throughout the paper, with the GaAs-based estimates of finite-size corrections separately stated.

III. RESULTS AND DISCUSSION

A. Relative stability of candidate defect structures

The significant number of basic structures that are possible for the As interstitial (at least seven, per Fig. 1), combined with the large number of local alloy environments that occur within an $In_{0.5}Ga_{0.5}As$ alloy (approaching $\sim 10^5$ possibilities, if one limits the local defect environment to only first- and second-nearest neighbors on the group-III sub-lattice), gives rise to a complex mix of stability behaviors whenever a given As-interstitial defect structure is inserted into a variety of sampled alloy environments and then subject to structural relaxation in a DFT calculation. Table I summarizes some of the complexities that are observed to arise.

As shown in the table, 25 unique combinations of defect structure and charge state were examined by DFT, with each combination sampled by either 54 or 72 different alloy configurations (each configuration being one of the 217-atom supercells whose construction was described in Section II.A). Following structural relation of each defect supercell using DFT, the final defect structure was compared with the initial defect structure to determine whether or not the initial structure was stable. Stable structures were defined as those in which the As interstitial atom moves by less than ≈0.05 nm during relaxation. All structures identified as unstable were subsequently visualized using CrystalMaker software [16] in order to determine the final, transformed defect structure produced by the DFT structural relaxation process. With only rare exceptions (a few percent of all configurations), the transformed structures were easily recognized as one of the seven original structures. In a few configurational instances of the initial C_{1h}-$p001_{III}$ q=0 As interstitial, a new C_{1h}-like structure was observed, as indicated

by the 'C_{1h}-new' designation shown in Table I. Relaxation of this new structure when placed in GaAs did not lead to a stable configuration, as the structure transformed to C_{1h}-bc_g in GaAs.

Of the 25 initial combinations of defect structure and charge state listed in Table I, only four combinations show complete stability for all sampled alloy configurations; six combinations show complete instability for all sampled alloy configurations; and the remaining 15 configurations show varying degrees of mixed stability, where some percentage of the sampled configurations have initial structures that persist during relaxation with the remaining configurations transforming to another defect structure. The right side of Table I summarizes the types of transformed defect structures that are produced whenever a given initial defect structure and charge state proves unstable during structural relaxation.

B. Mean formation energies and transition levels

Even though the mean formation energies do not entirely define the preferred ground states of the defect in an alloy, they still inform broad defect stability trends within the alloy. To explore these trends, we compute mean defect-formation energies for each of the 25 combinations of defect structure and charge state listed in Table I. For a given structure and charge state, the mean energy is based on only those initial configurations that remain stable; structures that transform from a different initial structure to reach the specific structure of interest are excluded from the averaging in order to avoid biasing the average toward lower energy structures. In addition, the averaging of sampled alloy configurations uses a weighting procedure to take into account degeneracies in the initial alloy sampling that come about because only unique first-neighbor configurations are included in the sampling procedures used to construct the initial sets of alloyed supercells containing the defects. Averaging procedures were applied to individual formation energies calculated for each alloy configuration using Eq. (2), with the calculations assuming As-rich conditions. Weighting for degeneracies has only a modest effect, producing < 20 meV differences relative to the unweighted means and standard deviations of the defect-formation energies. Parenthetically, we note that the mean and standard deviation of each defect's formation-energy distribution has direct relevance to the spatially random non-equilibrium population of defects created in the alloy immediately following a radiation-damage event. These purely statistical

parameters do not, however, describe the defect populations expected at thermal equilibrium. At thermal equilibrium in GaAs subject to As-rich conditions, the dominant ground-state defects are the As antisite (in p-type GaAs) and the Ga vacancy (in n-type GaAs), with As-interstitials lying ~2-3 eV higher in formation energy [12, 13, 17]. Because of the high formation energy of As interstitials relative to other intrinsic defects, the As interstitials will have negligible equilibrium concentrations at room temperature. Thus, assuming that InGaAs alloys are similar to GaAs, the importance of As interstitials will rest primarily with transient diffusion of non-equilibrium defect populations produced by radiation damage, and not with processes occurring near thermal-equilibrium.

Using the statistically computed mean formation energies, we constructed charge-state dependent formation-energy plots as a function of the Fermi level for the subset of initial defect structures that exhibited significant stability. Below, we consider each of these structures in turn, performing a bounds analysis of the transition levels observed in the plots in order to detect any inadmissible defect charge states. We also compare the mean formation energies in order to classify nominally stable and metastable regimes for each defect structure and charge state:

1. C_{2v}-110_a

Figure 3 plots the mean defect formation energy of the C_{2v}-110_a As interstitial as a function of the Fermi level for defects in the charge states q=-2, -1, 0, +1, and +2. The vertical lines in the plot located at ε_F=-0.06 eV and ε_F =0.86 eV are the lower and upper bounds on transition levels in 216-atom $In_{0.5}Ga_{0.5}As$ supercells, which we have replotted from the supercell-size-dependent bounds results shown in Fig. 2. We immediately see that the -2/-1 transition lies beyond the upper bound. Case-3 described in Section II.E applies, and the electron added to produce the q=-2 charge state of this defect is delocalizing when added to the finite-sized supercell. We conclude that q=-2 is not an admissible localized charge state for this defect. Note also that the -2/-1 transition slightly exceeds the upper bound. This effect results from the approximate character of the bounds when applied in smaller supercells, where *repulsion* of the added charge by the q=-1 charge already localized on the defect increases the energy slightly beyond that estimated in the idealized bounds calculation. In GaAs, where a similar, *but supercell-size-dependent*, bounds analysis of transition levels has been performed for the same C_{2v}-110_a defect, this residual

deviation from the bounds is seen to continuously decrease with increasing supercell size. This occurs because the larger supercells provide increasing volume that allows the delocalized electron to better minimize its interaction with charge already localized at the defect [14,15].

Examining Fig. 3 further, one sees that the +1/+2 transition level lies very close to the lower bound. Here we have Case 2 from Section II.E, but with the level positioned so close to the lower bound that delocalization is suggested. Despite this close proximity, however, the estimated fraction of delocalized charge remains quite small here (< 1%) because of the very flat slope of the lower bounds for all but the smallest supercell sizes (see Fig. 2). Thus, we cannot rule out the validity of this level based on the estimate of delocalized charge fraction alone. In GaAs, a similarly small deviation of this same level above the lower bounds is seen to continuously decrease with increasing supercell size [17], similar to the behavior noted above at the upper GaAs bounds. Analogous to the explanation given for the upper bounds, the hole added to produce the q=+2 charge state of this defect is delocalizing when added to the finite-sized supercell, but residual interaction again prevents the bounds from being exactly met. In contrast to the situation at the upper bound, however, the slight deviation of this level *within* the bounds indicates a residual *attractive* interaction of the delocalized hole and the localized q=+1 defect state. We tentatively assume that the size-dependence of this level in GaAs also obtains in $In_{0.5}Ga_{0.5}As$, such that the bounds analysis removes both q=±2 as admissible localized charge states for the C_{2v}-110_a As interstitial. Note that each combination of charge state and defect structure that is found to be an inadmissible localized state using the bounds analysis is indicated by the boldfaced entries shown in Table I.

Compared to the situation just seen for the lower bound, the interpretation of the 0/+1 and -1/0 levels appearing in Fig. 3 is unambiguous. Both of these levels are positioned above the very small Kohn-Sham gap, yet they remain in positions well below the upper bounds. Case-2 in Section II.E applies, and the estimated fraction of delocalized charge for both of these levels is < 4%. Because the delocalized charge fraction remains small and the bounds are not simultaneously nearby, we readily find that both levels involve valid localized charge states. Thus q=-1, 0, and +1 are allowed stable or metastable charge states for the C_{2v}-110_a As interstitial in $In_{0.5}Ga_{0.5}As$. For the same As interstitials in

GaAs, finite-size correction of 216-atom-supercell results to the infinite-supercell dilute limit yields corrections to the defect formation energy of -0.017, -0.043, and +0.065 eV, respectively [17]. Since similar-sized corrections are expected for $In_{0.5}Ga_{0.5}As$, we conclude that finite-size effects most likely have only minor importance for C_{2v}-110_a defects in the alloy.

As an aside, note that we have omitted discussion of the solid-blue curves shown in the bottom portion of Fig. 3. These curves plot relative probability distributions for each of the charge-state transition levels versus the Fermi level. These and similar distributions in Figs. 4-6 will be separately discussed in Section III.D, after we have examined variations in the defect formation energy arising from alloying.

2. C_{1h}-$p001_{III}$

Figure 4 plots the mean defect formation energy of the C_{1h}-$p001_{III}$ As interstitial as a function of the Fermi level for defects in the charge states q=0, +1, and +2. As seen above for the C_{2v}-110_a structure, we find transitions appearing at both the upper and lower bounds. Based on the bounds analysis discussion given above, the location of the 0/+1 transition level at the upper bounds (Case-3) indicates that the neutral charge state of this structure is inadmissible as a valid localized state. Similarly, the location of the +1/+2 transition at the lower bounds (Case-2; near to the bounds) indicates that the q=+2 charge state of this structure is also inadmissible as a valid localized state. For the transition nearest the lower bound, we again see a slight displacement of the transition level into the apparent gap such that the lower bound is not exceeded; as before, this suggests a residual attractive interaction of the delocalized hole with the hole already localized on the defect. As an aside, note that we omit analysis of the q=-1 C_{1h}-$p001_{III}$ data summarized in Table I because of the small number of stable defect configurations that are observed, which limits the reliability of the mean formation energy observed for this defect structure and charge state.

Thus, we are left with only q=+1 as a clearly allowed stable or metastable state for the C_{1h}-$p001_{III}$ As interstitial in $In_{0.5}Ga_{0.5}As$. Replotting the q=-1 state of the C_{2v}-110_a defect from Fig. 3 in Fig. 4 (as the green, short-dashed line), we see that the q=+1 state of the C_{1h}-$p001_{III}$ As interstitial becomes the ground state of the As interstitial for all Fermi levels located in the mid-gap region or below. For q=+1 C_{1h}-

$p001_{III}$ As interstitials in GaAs, finite-size correction of 216-atom-supercell results to the infinite-supercell dilute limit yields a correction to the defect formation energy of +0.033 eV [17]. As above, the small size of this correction in GaAs suggests that such corrections are of minor importance for statistical ensembles the C_{1h}-$p001_{III}$ defect in $In_{0.5}Ga_{0.5}As$.

3. T_d-III and T_d-As

Figure 5 plots the mean defect formation energy of the T_d-As and T_d-III As interstitials as a function of the Fermi level. As shown in Table I, the q=+3 charge states of both of these tetrahedral defects were remarkably stable during the DFT calculations of structural relaxation, with all initial configurations remaining stable. Reflecting this persistent stability, we see in Fig. 5 that the q=+3 charge state of the T_d-As defect becomes the formal ground state (prior to application of finite-size corrections) for a small range of Fermi levels located close to the valence-band edge.

Excepting the metastability of the q=+2 charge state for the T_d-As structure, which is seen in both Fig. 5 and Table I, no other charge states of the T_d structures were found to be stable or metastable. This partly resembles GaAs computations initiated with T_d-like defects where symmetry has been intentionally broken at the start of the calculation through a small initial displacement away from the fully symmetric position. In which case, it has been found that the T_d-As structure becomes unstable for q=+2, and the T_d-g structure becomes unstable for q=+1 [17].

For the T_d-As formation energies shown in Fig. 5, we find only one transition level, +2/+3, amenable to bounds analysis. Both charge states of this level are determined to be admissible because the level exhibits Case-2 behavior with the level located far from the bounds. Consistent with this interpretation, we find a small estimated fraction of delocalized charge of only 6 %. For the T_d-III As interstitial, calculations reveal an unusual case where there is only one non-transforming defect charge state, and no levels are available for bounds analysis. In such instances, the bounds analysis cannot provide any information and the defect necessarily remains admissible.

For q=+2 and +3 T_d-As and the q=+3 T_d-III As interstitials in GaAs, finite-size correction of 216-atom-supercell results to the infinite-supercell dilute limit yield corrections to the defect formation energy of +0.444, +0.820, and +0.858 eV [17]. Thus for these higher charge state defects, finite-size effects take

on consequential importance, as expected. After shifting the T_d defect-formation energies in Fig. 5 upwards by the indicated nominal correction values, the T_d-As and T_d-III structures become metastable states for all values of the Fermi level. This shift leaves the q=+1 C_{1h}-p001$_{III}$ As interstitial as the unambiguous ground state for Fermi levels below about mid gap, with the q=-1 C_{2v}-110$_a$ As interstitial remaining as the ground state for all Fermi levels above mid gap. These same ground states are seen by DFT in GaAs [17].

4. C_{3v}-hex

Figure 6 plots the mean defect formation energy of the C_{3v}-hex As interstitial as a function of the Fermi level for defects in the charge states q=0, +1, +2, and +3. Here, we find further similarities to the stability plots and bounds analyses already discussed. The 0/+1 transition lies exactly at the upper bound (Case 3), again indicating that the neutral charge state of the C_{3v}-hex structure is inadmissible as a localized state, Moreover, the +1/+2 transition lies just within the lower bound (Case 2; close to the bounds), indicating the q=+2 charge state is also inadmissible.

As seen in Table I, the q=+3 charged C_{3v}-hex structure has a strong tendency to spontaneously transform to other defect structures, indicating this defect is probably not valid. If we nonetheless use the mean energy of the 13% of initial configurations that remain stable, we find in Fig. 6 that the resulting +2/+3 transition rests just below the lower bounds. The slight shift to below the bounds could result simply from random error, caused by the statistically marginal sample size used to estimate the mean formation energy. Alternatively, the shift may again indicate a transition to a small repulsive residual interaction with the already-charged defect such that Case 3 applies. Thus, even those few configurations which do not transform structure are likely inadmissible.

As a result of the bounds analysis, only the q=+1 charge remains as an allowed localized state for the C_{3v}-hex structure. Comparing to the ground states for the C_{1h}-p001$_g$ and C_{2v}-110$_a$ structures that we have replotted in Fig. 6 (inclined solid-green lines), we find that the q=+1 state of the C_{3v}-hex structure is always metastable and not a ground state. This behavior matches that recently seen in GaAs for this structure, where q=+1 is also found as the only allowed metastable state [17]. For the q=+1 C_{3v}-hex As interstitials in GaAs, finite-size correction of 216-atom-supercell results to the infinite-supercell dilute

limit yields a correction to the defect formation energy of +0.097 eV [17]. The modest size of this correction in GaAs suggests that such corrections are of minor importance for statistical ensembles the C_{3v}-hex defect in $In_{0.5}Ga_{0.5}As$.

5. C_{1h}-bc_{III} and D_{2d}-001_a

As seen in Table I, the C_{1h}-bc_{III} structure remained stable during DFT structural relaxation for only 6-11% of the initial configurations sampled for the q=-1 and the q=0 charge states. Moreover, for q=+1, all of the initial configurations transformed to another structure. Because of the small number of stable defect configurations that were observed, the mean formation energies for this defect structure are less reliable, and we therefore do not present a stability plot or bounds analysis. The behavior of this defect in $In_{0.5}Ga_{0.5}As$ to a degree resembles with recent findings for GaAs, where the q=0 charge state of the C_{1h}-bc_g As interstitial is found to be a valid metastable state and the q=±1 charge states are unstable [17].

Lastly in Table I, we see that the D_{2d}-001_a structure very rarely remains stable for the examined q= -1, 0, and +1 charge states. This contrasts with recent findings for GaAs, where these charge states are each found to be metastable [17].

C. Variations in defect formation energy due to alloying

The significant tendency towards structural transformation during the DFT calculations, as seen in Table I, results in part from large variations in the defect formation energy produced by the varying local alloy environment. To characterize these variations, we computed the standard deviation of the defect formation energy for a subset of the 25 charge-state and defect-structure combinations given in Table I. This subset comprises defects reported in Figs. 3-6, excluding however, the charge states of each defect structure that were found to be inadmissible using the bounds analysis. The resulting subset contains eight combinations of charge state and defect structure that our analysis has indicated to be most significant for the As interstitial in $In_{0.5}Ga_{0.5}As$.

To visualize the formation-energy variations embodied by the calculated standard deviations, we constructed Fig. 7 and Fig. 8, where we plot relative distributions of defect energies that arise for the above-described significant defect states. To obtain these illustrative plots, we assume that the distribution of energies in the alloy is in each case reasonably well approximated by a Gaussian

distribution. For self-consistency, the formation-energy distribution for each structure and charge state is constructed assuming a Fermi level positioned at the valence band edge.

Figures 7(a) and 7(b) show resulting energy distributions for the C_{2v}-110_a and C_{1h}-$p001_{III}$ As-interstitials. Note that the standard deviation of the formation energy is large for all defects and charge states, ranging from 0.113 to 0.209 eV. For the important ground states of the As interstitial in $In_{0.5}Ga_{0.5}As$, q=+1 C_{1h}-$p001_{III}$ and q=-1 C_{2v}-110_a, we see local-ground-state energy distributions spanning a wide range of formation energies *approaching 1.2 eV* ($\pm 3\sigma$). These $\pm 3\sigma$ ranges are comparable to ranges separately found by differencing the DFT formation-energy extrema of the sampled defect populations (0.98 eV for q=-1 C_{2v}-110_a and 1.15 eV for q=+1 C_{1h}-$p001_{III}$), suggesting an approximately normal distribution of each population. These wide distribution ranges are similar to those found in a previous study for the As vacancy $In_xGa_{1-x}As$, where the authors use special quasirandom structures to study the effect of alloying on the vacancy formation energy [4].

Figures 8(a) and 8(b) show the energy distributions found for the T_d-III, C_{3v}-hex, and T_d-As interstitials. These distributions, while still quite wide, are less extreme than observed in Fig. 7, suggesting that the higher symmetry of these defects alters their coupling to the alloyed lattice or otherwise constrains their freedom to reconfigure.

For a given charge state, the observed variations in formation energy are seen to approach or exceed the separation of the mean formation energy of differing defect structures (the q=+1 distributions in Figs. 7(a), 7(b), and 8(a) are a good example). Because these distributions ultimately link to local variations in the group-III sub-lattice occupancy within the alloy, the defect structure that is *locally* most stable in the alloy is at times not the one implied by a simple comparison of mean formation energies for the basic structures. Thus, within a spatially random array of non-equilibrium point-defects formed by radiation-induced displacement damage, we can expect spontaneous transformation of some of the initial defect structures, just as we have seen in Table I. Local distortions of the lattice produced by alloying may also promote local structural transformations by eliminating symmetry-related local minima or saddle points that would otherwise preserve the local metastability of defects within the highly periodic lattices of unalloyed materials. Such effects offer a working hypothesis that may explain why higher

symmetry D_{2d}-001_a As interstitials have been found to be unstable herein for $In_{0.5}Ga_{0.5}As$, but are found to be metastable over a range of charge states in recent work on GaAs [17].

As a final point regarding alloy defect formation energies, note that the method used to construct our sets of alloyed supercell configurations (where six randomly sampled supercells have been made for each distinct set of group-III first neighbors) allows us to estimate how much the defect formation energy varies due to first-neighbors site occupancy versus the occupancy of more distant lattice sites. An example analysis of the variation in formation energy, performed *between and within* each set of first-neighbors, is shown in Table II for the q=-1 charge state of the C_{2v}-110_a defect. We find that the standard deviation between first-neighbor mean energies is σ=0.158 eV, while the average of standard deviations taken within first-neighbor sets (where variations in energy are only due to the changing random sampling performed beyond the first-neighbor sites) is σ=0.147 eV. For the q=+1 charge state of the C_{1h}-$p001_{III}$ defect, these two standard deviations are even closer to parity. We conclude that first-neighbor group-III site occupancy explains only about one-half of the variation in defect formation energy, with the rest of the variation resulting from the site occupancy of second-neighbors and more-distant group-III sites.

D. Variations in charge-state transition levels due to alloying

Given the large variations seen in the defect formation energy, it proves interesting to examine whether alloying produces similar variations in the charge-state transition levels of the defects. To this end, individual transition levels were calculated for each alloy configuration and charge-state transition wherein the defect-containing supercell retained the same defect structure before and after transition. For each defect level, a mean and standard deviation for the observed population of transitions was then computed, with a weighting procedure again applied to account for degeneracies. The analysis includes all fixed-defect-structure transitions including those with levels positioned near the bounds. To visualize the results, we again assume a normal distribution and then plot the relative probability of the transition level as a function of the Fermi level. These plots appear as the solid-blue curves in the bottom half of Figs. 3-6; each plot corresponds to one of the mean transition levels separately estimated in the upper half of each figure (marked by the solid circles). The plotted distributions are arbitrarily normalized such that the area under each curve is constant, and y-axis labelling is suppressed to simplify presentation.

The energy variation of the transition levels is seen to depend on the position of the level relative to the bounds, with levels near the lower bound exhibiting the narrowest distributions (σ=0.003-0.015 eV), with levels near the upper bound exhibiting somewhat broader distributions (σ=0.012-0.029 eV), and with levels far from both bounds exhibiting the broadest distributions (σ=0.044-0.071 eV). It proves revealing to compare to variations arising in the bounds themselves as a result of the randomly varying bulk-supercell compositions about the mean of x=0.5. Calculations of the bounds for 50 different 216-atom bulk-alloy supercells show the standard deviation of the lower and upper bounds to be 0.002 and 0.022 eV, respectively. Comparing these values to the standard deviations of the levels, we see that levels near to the bounds tend to pin to the bounds such that the variability of the level approaches that of the bounds. One clear exception to this trend is the 0/+1 transition of the C_{3v}-hex defect structure where σ=0.012 eV for the defect level is *much less* than σ=0.022 eV for the bounds. This unphysical exception is easily understood as a likely statistical artifact that arises because only 6 of the 54 sampled configurations of the C_{3v}-hex defect completed the 0/+1 charge-state transition without structurally transforming to a different symmetry.

For the 0/+1 and the -1/0 C_{2v}-110_a transitions in Fig. 3 and the +2/+3 T_d-As transition in Fig. 5, the bounds are remote from the levels, and we can see the effect of alloying independent of strong interaction with the bounds. Comparing to the C_{2v}-110_a and T_d-As defect-formation energies in Figs.7 and 8, we see that the energy variation of these levels is reduced to about 1/3-1/2 times that of the underlying formation energies. This reduction is expected given that the levels involve an energy difference taken between pairs of atomically similar alloy configurations of the same composition, with the common atomic structures producing correlation of the differenced formation energies.

IV. CONCLUSION

We have examined the atomic structure, defect formation energies, and charge-state transition levels for 25 different combinations of defect structure and charge state for As interstitials in $In_{0.5}Ga_{0.5}As$ alloy. Aided by our bounds-analysis approach, which efficiently identifies valid and invalid defect charge states, eight of these combinations were found to be significant metastable or stable defect states of the As

interstitial. Comparing the resulting mean formation energies and transition levels to those of GaAs, we find clear similarities, with the q=+1 C_{1h}-p001$_{III}$ and the q=-1 C_{2v}-110$_a$ As interstitials appearing as the most important ground states in both $In_{0.5}Ga_{0.5}As$ and GaAs. The broadly similar results obtained for As interstitials in these two closely related materials suggests that DFT/LDA and our bounds-analysis approach yield reasonable defect properties even in the presence of the large band-gap error for $In_{0.5}Ga_{0.5}As$. Further supporting this view, Komsa and Pasquarello also find very similar defect-formation energies and levels in $In_{0.5}Ga_{0.5}As$ versus GaAs for related hybrid functional studies of Ga and As vacancies and antisites, where in contrast to present work, band-gap error is absent [5].

Through statistical sampling of the local alloy environment, we find remarkably large variations in the As-interstitial defect formation energy as the local occupancy of the group-III sub-lattice varies. Formation energies are calculated to span a range that approaches 1.2 eV ($\pm 3\sigma$), depending on the defect structure and charge state. This resembles previous work on the As vacancy in $In_xGa_{1-x}As$ by Murphy *et al.*, where the formation energy of the vacancy was found to span 0.6 to 1.3 eV, with the span depending on alloy composition [4]. For the As interstitial in $In_{0.5}Ga_{0.5}As$, we find that the observed variations of formation energy depend upon both first-neighbor and second-neighbor group-III site occupancies, with adjacent sites beyond the second neighbors also having possible significance. Variations in transition levels for defects with only localized charge states (*i.e.*, those levels located far from the bounds) are ~1/3 to 1/2 the variations of the underlying defect formation energies. The reduced variation of the levels arises from the differencing of correlated formation energies for atomically similar defects in adjacent charge states, as needed to obtain the level for each sampled alloy configuration. In closing, we note that the observed dependence of defect properties on the local alloy environment fundamentally alters defect-diffusion pathways in a manner not captured by existing transport models for unalloyed materials [11,12].

ACKNOWLEDGEMENTS

Sandia National Laboratories is a multi-program laboratory managed and operated by Sandia Corporation, a wholly owned subsidiary of Lockheed Martin Corporation, for the U.S. Department of Energy's National Nuclear Security Administration under contract DE-AC04-94AL85000.

REFERENCES

[1] A. Carvalho, J. Coutinho, R. Jones, J. Goss, M Barroso, and P. R. Briddon, Phys. Rev. B **78**, 125208 (2008).

[2] A. Chroncos, H. Bracht, C. Jiang, B. P. Uberuaga, and R. W. Grimes, Phys. Rev. B **78**, 195201 (2008).

[3] A. Amore Bonapasta and P. Giannozzi, Phys. Rev. Lett. **84**, 3923 (2000).

[4] S. T. Murphy, A. Chroneos, R. W. Grimes, C. Jiang, and U. Schwingenschl□gl, Phys. Rev. B **84**, 184108 (2011).

[5] H.-P. Komsa and A. Pasquarello, Physica B **407**, 2833 (2012).

[6] T. V. Bezyazychnaya, M. V. Bogdanovich, A. V. Grigor'ev, V. M. Zelenkovskii, V .V. Kabanov, D. M. Kabanov, Y. V. Lebiadok, A. G. Ryabtsev, G. I. Ryabtsev, and M. A. Shchemelev, Physics of the Solid State **55**, 2165 (2013).

[7] L. M. R. Scolfaro, R. Pintanel, A. Fazzio, and J. R. Leite, Int. J. Quant. Chem: Quant. Chem. Symp. **27**, 213 (1993).

[8] T. Obata, J. Iwata, K. Shiraishi, and A. Oshiyama, J. Cryst. Growth **311**, 2772 (2009).

[9] L. E. Ramos, J. Furthmüller, F. Bechstedt, L. M. R. Scolfaro, and J. R. Leite, J. Phys.: Condens. Matter **14**, 2577 (2002).

[10] V. Popescu and A. Zunger, Phys. Rev. B **85**, 085201 (2012).

[11] S. M. Myers, P. J. Cooper, and W. R. Wampler, J. Appl. Phys. **104**, 044507 (2008).

[12] W. R. Wampler and S. M. Myers, J. Appl. Phys. **117**, 045707 (2015).

[13] P. A. Schultz and O. A. von Lilienfeld, Modelling Simul. Mater. Sci. Eng. **17**, 084007 (2009).

[14] N. A. Modine, A. F. Wright, and S. R. Lee, Computational Materials Science **92**, 431 (2014).

[15] A. F. Wright and N. A. Modine, Phys. Rev. B **91**, 014110 (2015).

[16] Crystallographic images generated using CrystalMaker®: a crystal and molecular structures program for Mac and Windows. CrystalMaker Software Ltd, Oxford, England (www.crystalmaker.com).

[17] A. F. Wright and N. A. Modine (unpublished). Supercell-size corrections in this work were determined through least-squares fitting of the formation energies computed for defects inserted into 216-atom, 512-atom, and 1000-atom supercells. The physically motivated polynomial fits included constant, $1/L$, and $1/L^3$ terms based on the work of Makov and Payne (see Ref. 44). For each defect, the $1/L$ term's coefficient was determined from q, Madelung's constant, and the dielectric constant of GaAs, with the $1/L^3$ term's coefficient and the dilute-limit formation energy separately determined by the fitting. Selected results from this work on defect properties in GaAs appear in Ref. 12.

[18] For the C_{3v}-hex and T_d-As defect structures, related but modified procedures were used to build the alloyed supercells.

[19] http://dft.sandia.gov/socorro.

[20] P. Hohenberg and W. Kohn, Phys. Rev. B **136**, 864 (1964).

[21] W. Kohn and L. J. Sham, Phys. Rev. **140**, A1133 (1965).

[22] D. M. Ceperley and B. J. Alder, Phys. Rev. Lett. **45**, 566 (1980).

[23] http://www.fhi-berlin.mpg.de/th/fhi98PP/. Three electrons were treated as valence ($4s_2$ and $4p_1$) for Ga and five electrons ($4s_2$ and $4p_3$) for As. Cutoff radii of 1.10, 1.30, and 2.25 Bohr were used for the *s*, *p*, and *d* channels of Ga and 1.00, 1.18, and 1.80 Bohr were used for As. Radii of 1.20 and 1.00 Bohr were used for Ga and As, respectively, to generate the partial core charges.

[24] L. Kleinman and D. M. Bylander, Phys. Rev. Lett. **48**, 1445 (1982). The projectors were constructed using the *s* semilocal NCP as the local potential.

[25] D. R. Hamann, Phys. Rev. B **40**, 2980 (1989). Three electrons were treated as valence ($5s_2$ and $5p_1$). Cutoff radii of 1.26, 1.40, 1.87, and 1.10 Bohr were used for the *s*, *p*, *d* and *f* channels. A radius of 1.80 Bohr was used to generate the partial core charge.

[26] S. G. Louie, S. Froyen, and M. L. Cohen, Phys. Rev. B **26**, 1738 (1982).

[27] J. Ihm, A. Zunger, and M. L. Cohen, J. Phys. C **12**, 4409 (1979).
[28] H. J. Monkhorst and J. D. Pack, Phys. Rev. B **13**, 5188 (1976).
[29] Y. Bar-Yam and J. D. Joannopoulos, Phys. Rev. B **30**, 1844 (1984).
[30] F. D. Murnaghan, Proc. Natl. Acad. Sci. U.S.A. **30**, 244 (1944).
[31] O. Madelung (Editor), *Semiconductors - Basic Data*, 2nd Edition, (Springer-Verlag, Berlin, 1996), p. 104.
[32] O. Madelung (Editor), *Semiconductors - Basic Data*, 2nd Edition, (Springer-Verlag, Berlin, 1996), p. 136.
[33] J. Donohue, *The Structures of the Elements* (Wiley, New York, 1974).
[34] S. B. Zhang and J. E. Northrup, Phys. Rev. Lett. **67**, 2339 (1991).
[35] C. G. Van de Walle, D. B. Laks, G. F. Neumark, and S. T. Pantelides, Phys. Rev. B **47**, 9425 (1993).
[36] C. Freysoldt, B. Grabowski, T. Hickel, J. Neugebauer, G. Kresse, A. Janotti, and C. G. Van de Walle, Rev. Mod. Phys. **86**, 253 (2014).
[37] A. Alkauskas, P. Broqvist, and A. Pasquarello, Phys. Stat. Sol. B **248**, 775 (2011).
[38] C. D. Latham, M. Alatalo, R. M. Nieminen, R. Jones, S. Oberg, and P. R. Bridden, Phys. Rev. B **72**, 235205 (2005).
[39] The bounds were obtained from Eqs. 5 and 6 by performing a series of DFT calculations using a single 216-atom bulk-$In_{0.5}Ga_{0.5}As$ supercell into which a fixed charge, Δq, was added (or removed) in each of the following amounts: 0.01, 0.02, 0.05, 0.1, 0.2, 0.5, 1.0, 2.0, 5.0, 10.0, and 20.0 electrons. The *equivalent* one-electron supercell size is in each case given by $216/\Delta q$, as this quantity yields the correct one-electron charge density at each supercell size of interest. K-point sampling ranged from 5×5×5 up to 12×12×12 depending on the amount of added or removed charge, with sampling chosen to yield k-point convergence of the bounds to within ~ 10 meV or less.
[40] E. Burstein, Phys. Rev. **93**, 632 (1954).
[41] T. S. Moss, Proc. Phys. Soc. B **67**, 775 (1954).
[42] C. P. Kuo, S. K. Vong, R. M. Cohen, G. B. Stringfellow, J. Appl. Phys. **57**, 5428 (1985).
[43] M. Leslie and M. J. Gillan, J. Phys. C **18**, 973 (1985).
[44] G. Makov and M.C. Payne, Phys. Rev. B **51**, 4014 (1995).
[45] C. W. M. Castleton and S. Mirbt, Phys. Rev. B **70**, 195202 (2004).
[46] C. W. M. Castleton, A. Höglund, and S. Mirbt, Phys. Rev. B **73**, 035215 (2006).
[47] S. Lany and A. Zunger, Phys. Rev. B **78**, 235104 (2008).
[48] C. Freysoldt, J. Neugebauer, and C. G. Van de Walle, Phys. Lett. **102**, 016402 (2009).
[49] N. D. M. Hine, K. Frensch, W. M. C. Foulkes, and M. W. Finnis, Phys. Rev. B **79**, 024112 (2009).
[50] S. E. Taylor and F Bruneval, Phys. Rev. B **84**, 075155 (2011).
[51] H.-P. Komsa, T. T. Rantala, and A. Pasquarello, Phys. Rev. B **86**, 045112 (2012).
[52] Y. Kumagai and F. Oba, Phys. Rev. B **89**, 195205 (2014).
[53] S. Adachi, *Physical Properties of III-V Semiconductor Compounds* (Wiley-VCH, Weinheim, 2004), p. 66.

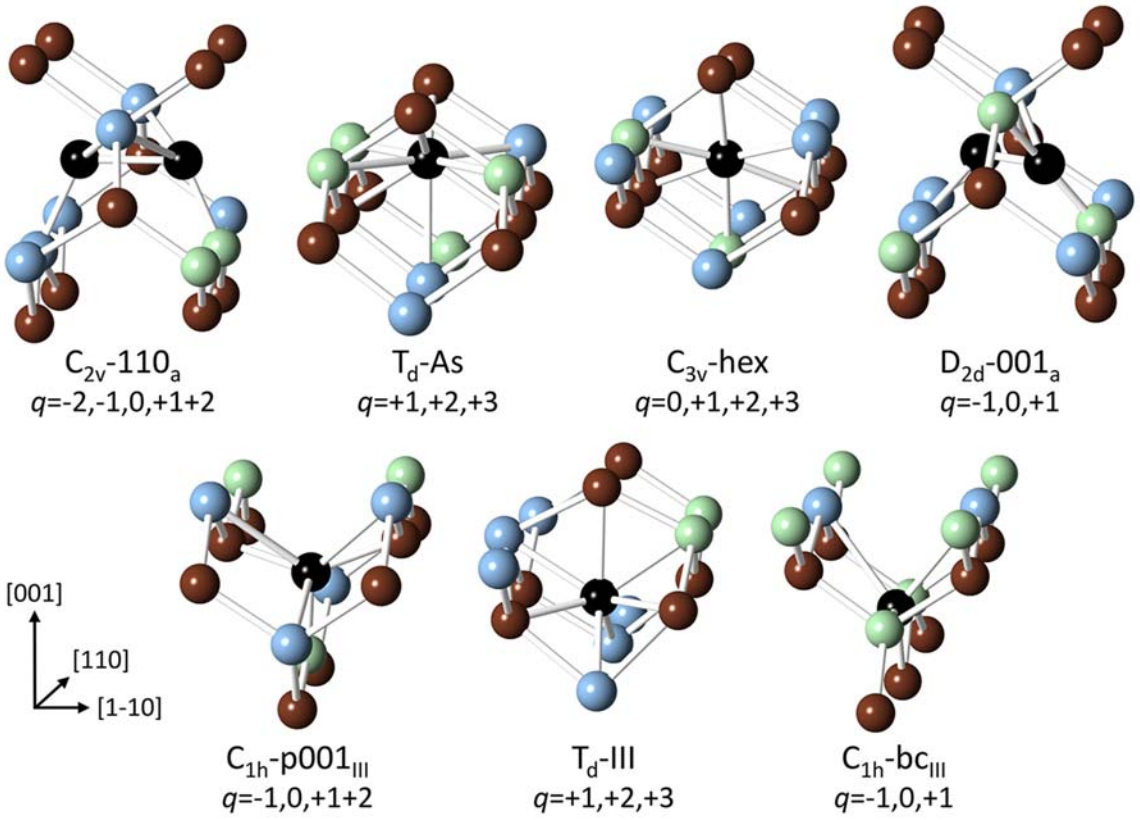

Figure 1. (Color online) Ball-and-stick models of candidate As-interstitial defect structures in InGaAs alloys. The black balls indicate interstitial As atoms; the dark-grey balls (brown online) indicate As atoms located on the group-V sub-lattice; and the light-grey balls (light-green and light-blue online) indicate Ga and In atoms located on the group-III sub-lattice. DFT calculations were performed for each defect structure for each of the indicated charge states, q.

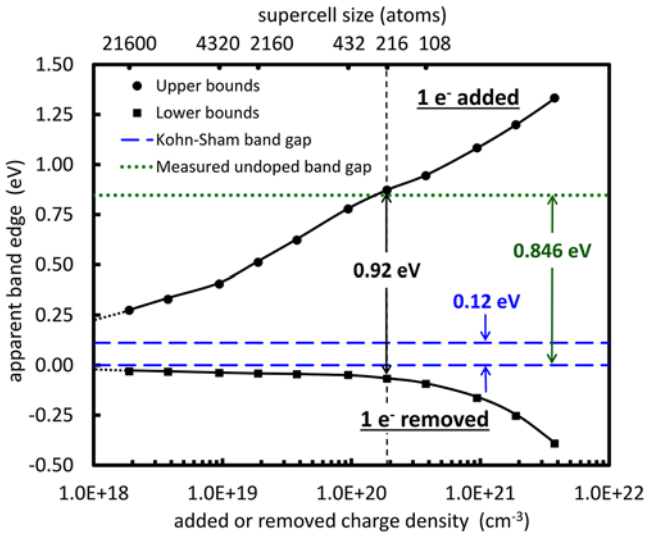

Figure 2. (Color online) Upper and lower bounds on admissible localized defect levels in $In_{0.5}Ga_{0.5}As$ versus the size of the finite periodic supercell (upper axis) used for DFT calculations of defect levels. The added or removed charge densities (lower axis) result when 1 electron is either added to or removed from each of the corresponding finite-sized bulk-alloy supercells. The bounds are compared to the Kohn-Sham band gap (blue long-dashed line) and the measured band gap (green dotted line) in undoped $In_{0.5}Ga_{0.5}As$.

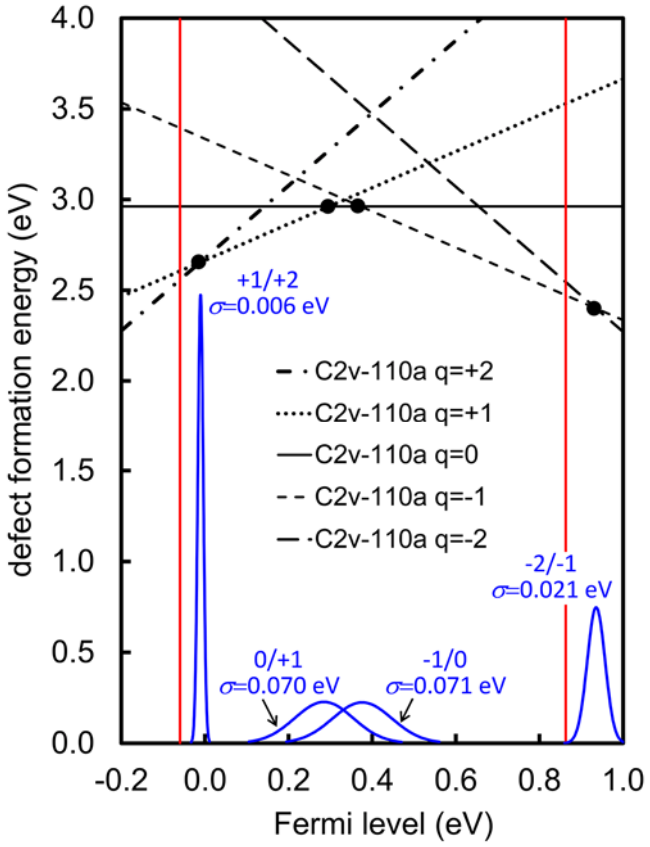

Figure 3. (Color online) Mean defect-formation energies vs. Fermi level for the C_{2v}-110_a split As interstitial in $In_{0.5}Ga_{0.5}As$ with charge states q=-2, -1, 0, +1, and +2. Calculated lower and upper bounds on defect charge-transition levels in $In_{0.5}Ga_{0.5}As$ are indicated by the solid vertical red lines located at ε_F=-0.06 eV and ε_F =0.86 eV. Black dots indicate the charge-state transition levels of the defect given by intersection of the mean formation energies; corresponding solid-blue Gaussian curves show relative probability distributions of the defect levels as obtained from a separate statistical analysis of the population of levels found for each set of sampled alloy configurations; σ indicates the standard deviation of each distribution.

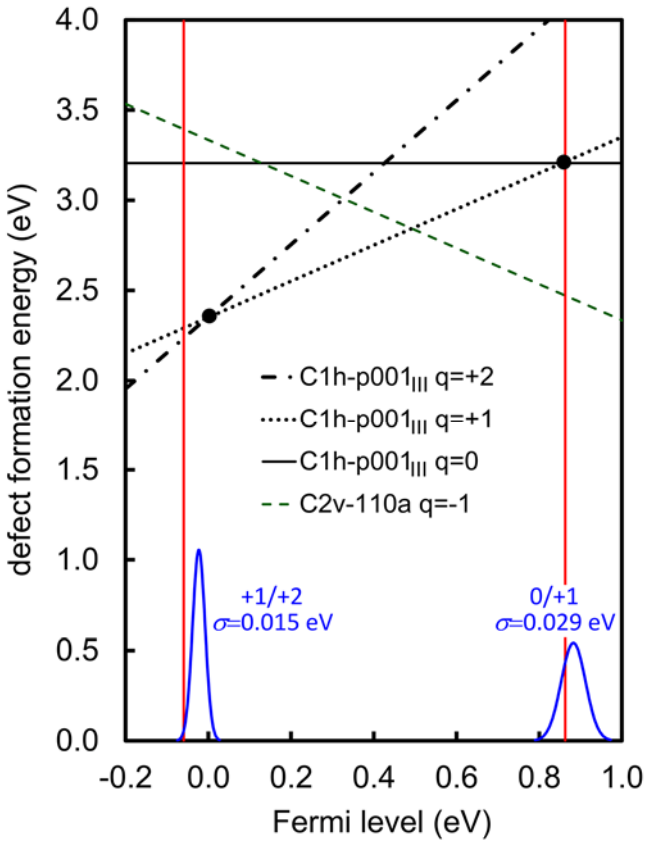

Figure 4. (Color online) Mean defect-formation energies vs. Fermi level for the C_{1h}-$p001_{III}$ As interstitial in $In_{0.5}Ga_{0.5}As$ with charge states q= 0, +1, and +2. Calculated lower and upper bounds on defect charge-transition levels in $In_{0.5}Ga_{0.5}As$ are indicated by the solid vertical red lines located at ε_F=-0.06 eV and ε_F =0.86 eV. Black dots indicate the charge-state transition levels of the defect given by intersection of the mean formation energies; corresponding solid-blue Gaussian curves show relative probability distributions of the defect levels as obtained from a separate statistical analysis of the population of levels found for each set of sampled alloy configurations; σ indicates the standard deviation of each distribution. The q=-1 C_{2v}-110_a ground state is replotted (inclined short-dashed green line) from Fig. 3 for comparison.

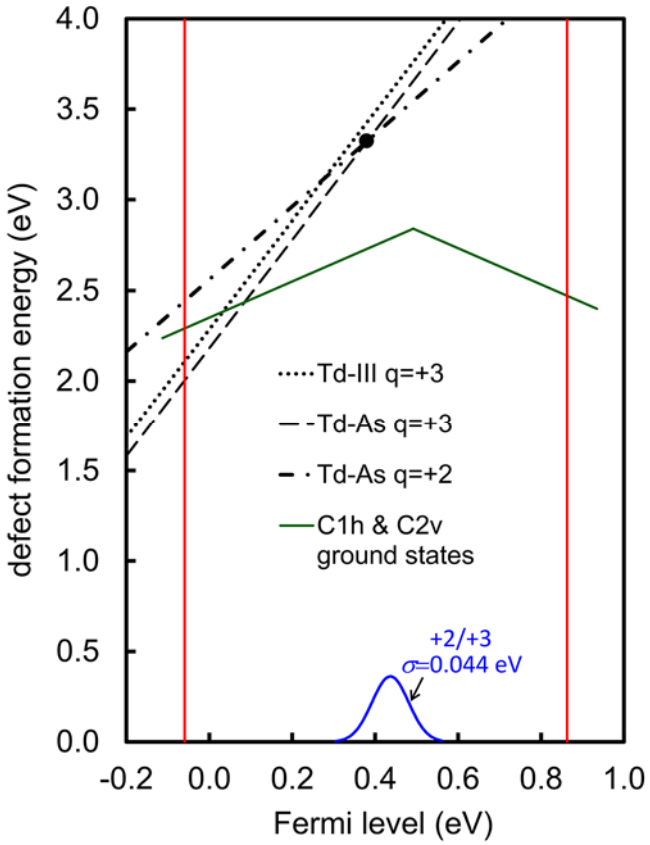

Figure 5. (Color online) Mean defect-formation energies vs. Fermi level for the T_d-III As interstitial (q=+3) and the T_d-As interstitial (q= +2 and +3) in $In_{0.5}Ga_{0.5}As$. Calculated lower and upper bounds on defect charge-transition levels in $In_{0.5}Ga_{0.5}As$ are indicated by the solid vertical red lines located at ε_F=-0.06 eV and ε_F =0.86 eV. Black dots indicate the charge-state transition levels of the defect given by intersection of the mean formation energies; corresponding solid blue curves show relative probability distributions of the defect levels as obtained from a separate statistical analysis of the population of levels found for each set of sampled alloy configurations; σ indicates the standard deviation of each distribution. Ground states of the q=+1 C_{1h}-$p001_{III}$ and q=-1 C_{2v}-110_a defects are replotted (lower inclined solid green lines) from Figs. 3 and 4 for comparison.

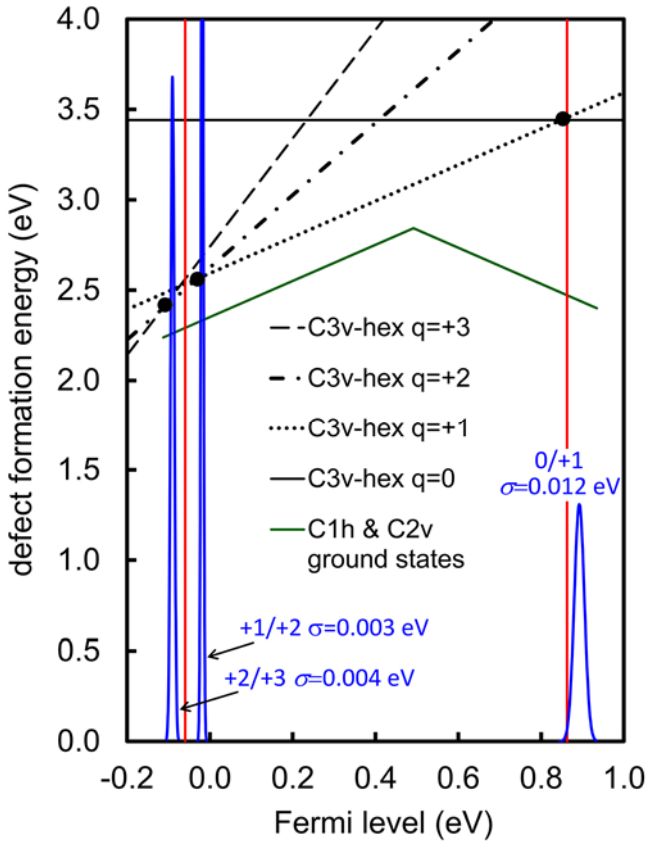

Figure 6. (Color online) Mean defect-formation energies vs. Fermi level for the C_{3v}-hex As interstitial in $In_{0.5}Ga_{0.5}As$ with charge states q=0, +1, +2, and +3. Calculated lower and upper bounds on defect charge-transition levels in $In_{0.5}Ga_{0.5}As$ are indicated by the solid vertical red lines located at ε_F=-0.06 eV and ε_F =0.86 eV. Black dots indicate the charge-state transition levels of the defect given by intersection of the mean formation energies; corresponding solid-blue Gaussian curves show relative probability distributions of the defect levels as obtained from a separate statistical analysis of the population of levels found for each set of sampled alloy configurations; σ indicates the standard deviation of each distribution. Ground states of the q=+1 C_{1h}-$p001_{III}$ and q=-1 C_{2v}-110_a defects are replotted (lower-most inclined solid green lines) from Figs. 3 and 4 for comparison.

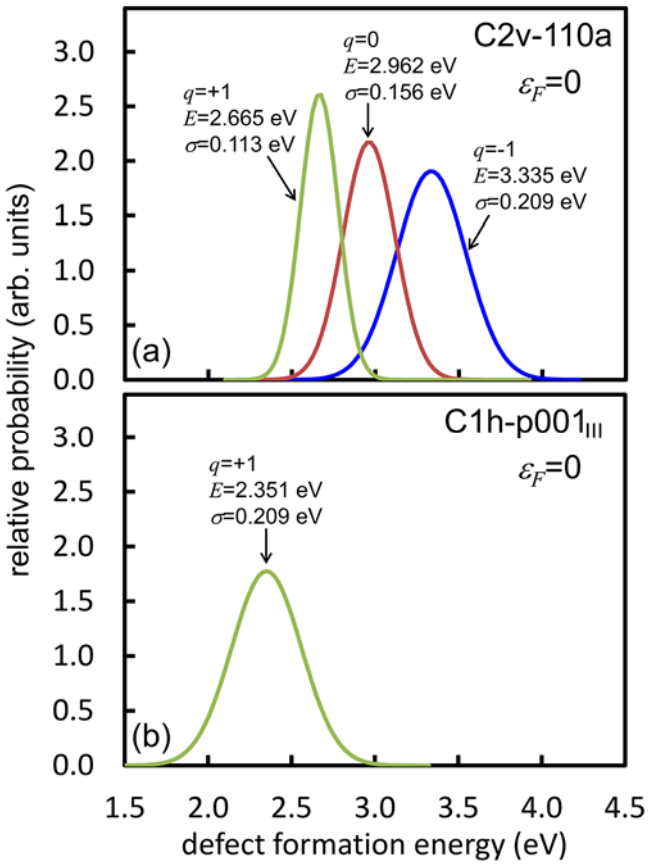

Figure 7. (Color online) Relative probability distribution of the defect formation energy for (a) C_{2v}-110_a and (b) C_{1h}-$p001_{III}$ As-interstitial defect structures in $In_{0.5}Ga_{0.5}As$. The formation-energy distributions are computed for a Fermi level located at the valence band maximum (ε_F=0).

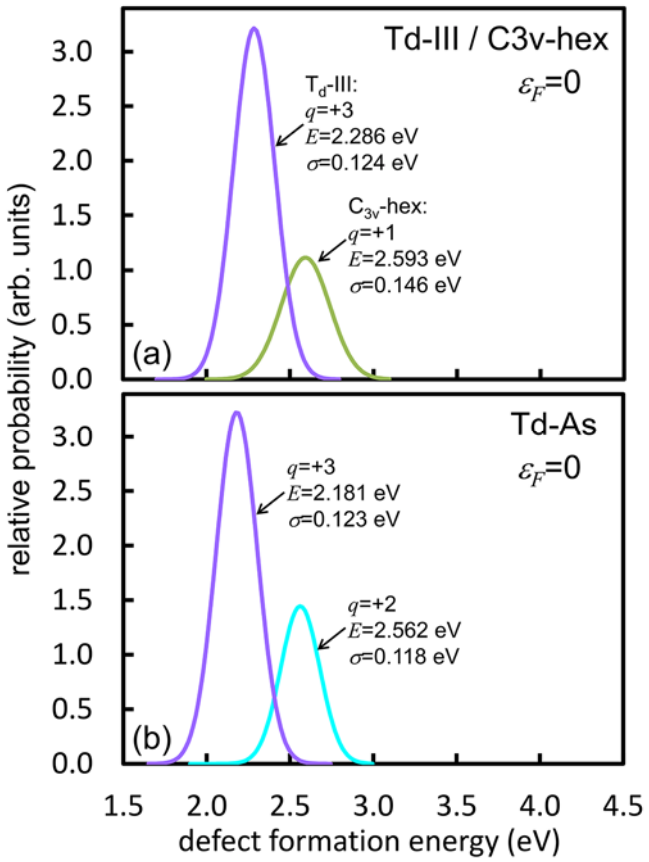

Figure 8. (Color online) Relative probability distribution of the defect formation energy for (a) T_d-III and C_{3v}-hex, as well as (b) T_d-As interstitial defect structures in $In_{0.5}Ga_{0.5}As$. The formation-energy distributions are computed for a Fermi level located at the valence band maximum (ε_F=0).

initial defect structure	number of sampled configura-tions	percentage of sampled configurations which are not transformed by structural relaxation						transformed defect structures produced by structural relaxation (ordered by likelihood of occurrence)					
	n	q=-2	q=-1	q=0	q=+1	q=+2	q=+3	q=-2	q=-1	q=0	q=+1	q=+2	q=+3
C_{2v}-110_a	54	**100%**	100%	85%	74%	**76%**		none	none	C_{1h}-bc_{III} **C_{1h}-p001$_{III}$** **C_{3v}-hex**	C_{1h}-p001$_{III}$ C_{3v}-hex	**C_{1h}-p001$_{III}$** **C_{3v}-hex** Td-As	
C_{1h}-p001$_{III}$	72		13%‡	**43%**	93%	**85%**			C_{2v}-110_a C_{1h}-bc_{III}	C_{2v}-110_a C_{1h}-bc_{III} C_{1h}-new	C_{3v}-hex	**C_{3v}-hex**	
T_d-As	72				0%	43%	100%				C_{3v}-hex C_{1h}-p001$_{III}$	**C_{3v}-hex** **C_{1h}-p001$_{III}$**	none
T_d-III	54				0%	0%	100%				C_{1h}-p001$_{III}$ C_{3v}-hex	**C_{3v}-hex** **C_{1h}-p001$_{III}$**	none
C_{3v}-hex	54			**11%**	41%	**33%**	**13%**			C_{2v}-110_a **C_{1h}-p001$_{III}$** C_{1h}-bc_{III}	C_{1h}-p001$_{III}$	**C_{1h}-p001$_{III}$** T_d-As	**C_{1h}-p001$_{III}$** T_d-As T_d-III
C_{1h}-bc_{III}	72		6%	17%	0%				C_{2v}-110_a C_{1h}-p001$_{III}$	**C_{1h}-p001$_{III}$** C_{2v}-110_a	C_{1h}-p001$_{III}$ C_{2v}-110_a C_{3v}-hex		
D_{2d}-001_a	54		0%	2%	0%				C_{2v}-110_a C_{1h}-p001$_{III}$	C_{2v}-110_a **C_{1h}-p001$_{III}$** **C_{3v}-hex**	C_{1h}-p001$_{III}$ C_{2v}-110_a C_{3v}-hex		

Table I. Variations in the structural stability of candidate defect structures and charge states in $In_{0.5}Ga_{0.5}As$: types of As-interstitial defect structures that were constructed (column 1); the number of random-alloy configurations, n, that were sampled for each structure (column 2); the percentage of sampled configurations that remained stable during structural relaxation for each defect charge state, q, that was examined (columns 3-8); and the types of transformed defect structures that were observed following structural relaxation, again for each defect charge state that was examined (columns 9-14). Boldfaced entries indicate either initial defect structures (columns 3-8), or transformed defect structures (columns 9-14), where the indicated charge state is not an admissible localized state of the structure according to our bounds analysis. ‡The small number of surviving configurations of the q=-1 C_{1h}-p001$_{III}$ defect, combined with wide variations in the few available formation energies, prevented bounds analysis of the -1/0 level; however, the inadmissibility of the q=0 charge state found by bounds analysis of the adjacent 0/+1 level suggests that the q=-1 state is inadmissible as well.

1st-neighbor site occupations defining each 1st-neighbor set				site-occupation degeneracy	number of randomized supercell configurations prepared	average defect-formation energy (taken within each 1st-neighbor set)	standard deviation of formation energy (taken within each 1st-neighbor set)
site *1*	site *2*	site *3*	site *4*			(eV)	(eV)
Ga	Ga	Ga	Ga	1	6	3.051	0.254
Ga	Ga	Ga	In	2	6	3.151	0.161
In	Ga	Ga	Ga	2	6	3.269	0.159
In	Ga	Ga	In	4	6	3.327	0.091
In	In	Ga	Ga	1	6	3.220	0.163
In	In	Ga	In	2	6	3.352	0.144
Ga	Ga	In	In	1	6	3.485	0.139
In	Ga	In	In	2	6	3.582	0.205
In	In	In	In	1	6	3.580	0.098
standard deviation taken between 1st-neighbor averages (eV):						0.158	
average of within-1st-neighbor standard deviations (eV):							0.147
global mean and standard deviation of formation energy (eV):						3.335	0.209

Table II. Sources of variation for the defect formation energy of the q=-1 C_{2v}-110_a As interstitial: Standard deviations computed *within* first-neighbor sets reflect the variance introduced by the six random far-field samples made for each set. The standard deviation computed *between* the mean energies of the first-neighbor sets reflects the variance introduced by differences in first neighbors. Weighting has been applied to account for the 1st-neighbor site-occupation degeneracies.